Chapter 4

Novel Electrical and Magnetic Properties of Double Perovskites $Eu_{2-x}Tb_xCoMnO_6$ (x = 0.0 and 1.0)

4.1 Introduction

To fulfil the requirement of daily need of technical devices the materials with coupled electrical and magnetic properties have become very interesting due to their astonishing multifunctional behavior [127,129,180,181]. The perovskite oxide (ABO_3) family reveals as good candidates for both ferroelectric and ferromagnetic but difficulties arise in the coupling of both ferroic orderings [17,182,183]. Based on density function calculation some authors predicted that polarization in magnetic perovskites may take place by substitution of different ions on A-site [143,184]. For the case, a smaller A-site ion induces the structural strain and these structural strains relaxed by the off-centering displacement of atoms and the tilting of BO_6 octahedral. Thus, the frustrations generated by octahedral tilting and off-centering leads to A-site disorder-driven ferroelectricity [143,185]. Similarly, a smaller B atom leads to B-site driven ferroelectricity via off-centering [186,187]. In this outline, the effects of the disorder in the rare-earth-based oxides having double perovskite (DP) structure $R_2BB'O_6$, where R is the rare earth metal ions while B and B' are transition metal ions, have become as an appropriate candidate for multi-functional devices [188–190]. The recent studies on various DPs shows various interesting properties viz., spin-reorientation, ferri-magnetic mott-insulating state, defect-induced modulation of physical properties, half-metallic phase, magnetocaloric effect, pyro current, exchange bias, large magneto-capacitance, tunable magnetization steps, giant magneto-resistance, colossal magneto-dielectric, cationic ordering, local atomic disorder and anti-phase domains, Griffiths-like phase, spin-phonon coupling, etc [5,6,39,41–43,45,47,53,139,142,191–208]. The DPs with non-magnetic A-site (like La, Y, Lu, Eu) were attractive since the only magnetic interaction behind it is the exchange interaction of transition

metal ions [5,122,152,153,209,210]. One of the interesting features exhibited by these DPs is meta-magnetic-transition (MMT) and can be used for solid-state refrigerators [135,211].

Beforehand, the extra-ordinary magnetic property of Eu_2CoMnO_6 (ECMO) has been reported elaborately [211]. It has been seen that ECMO shows MMT along with spin-phonon coupling. Moreover, the existence of glassy nature, Griffith's phase, double band-gap and Hopkinson-like has been observed. In this chapter, we desire to see the effect of partial exchange of non-magnetic ion (Eu^{3+}) with high moment magnetic ion (like Tb^{3+}). Thus, we have investigated the comparative study of DPs $Eu_{2-x}Tb_xCoMnO_6$ (with x = 0.0 and 1.0) and results are tried to compare with Tb_2CoMnO_6 (TCMO) [212–214]. The one end member of this series is $TbMnO_3$, with an orthorhombic and room temperature spiral magnetic structure that has been proposed to show the induced ferroelectricity [215–217]. The induced polarization was might be due to spin ordering where magnetic field displaced the ions, causing lattice strain and thus engenders electric polarization [218–220]. Furthermore, the partial Co substitution on Mn-site enhanced the ferromagnetic ordering of $TbMnO_3$ [221]. However, another member $EuMnO_3$ has similar crystallography as $TbMnO_3$, along with an incommensurate antiferromagnetic and *A*-type antiferromagnetic ordering as well as it is a multiferroic candidate [154,222–224]. The partial replacement of Mn with Co increases the anti-ferromagnetic ordering temperature of $EuMnO_3$ up to 50% [152]. Thus, incorporation of Tb, Eu, Mn and Co together may lead to interesting magnetic and dielectric properties.

4.2 Experimental

The polycrystalline DPs $Eu_{2-x}Tb_xCoMnO_6$ (x = 0.0 and 1.0, named as ECMO and ETCMO) were synthesized via standard solid-state reaction technique. The stoichiometric

mixture of high-purity Eu_2O_3, Tb_4O_7, CoO and Mn_2O_3 was used as starting material and similar steps were made as in our earlier report [211]. For the crystal structure information of the samples, the powder X-ray diffraction (XRD) patterns were recorded using Rigaku Miniflex II X-ray diffractometer (Cu-Kα). The analyses of XRD pattern were made using Rietveld refinement method through FULLPROF suite software. The dielectric property measurements were carried out using Keysight E4980A Precision LCR meter coupled with a He-based closed cycle refrigerator (CCR). The electrical DC resistivities were measured using a Keithley 6517B Electrometer with the standard 2-probe method. The magnetic properties were measured via MPMS3 magnetometer.

4.3 Results and discussions

4.3.1 Structural analysis

The XRD patterns of ECMO and ETCMO taken at room temperature are shown in Fig. 4.1. Most of the DPs $R_2BB'O_6$, usually crystallize either in a disordered orthorhombic phase [152,213] with space group *Pnma* where B/B' ions randomly occupied over 6c-sites or in a perfect ordered monoclinic phase [210,212] with space group P21/n (which is a subgroup of *Pnma*) where ions are distributed over Wyckoff positions 2c and 2d. There is a huge probability that in the ordered state itself, some of the B and B' ions interchange their crystallographic sites depending upon preparation conditions like sintering temperature atmosphere, heating and cooling rate, Valence states of cations and anions etc., and leads to some disordering. Generally, all the Co-Mn-based DPs exhibit prominent Co^{2+}, Co^{3+}, Mn^{3+}, and Mn^{4+} as the redox potentials difference between Co^{2+}–Mn^{4+} and Co^{3+}–Mn^{3+} couples are very small [225]. Other than this, Co^{2+} and Mn^{4+} ions may cause internal strain arising from the differences in

the ionic radii of Co^{2+} and Mn^{4+} which also can make promising mix vacancies. Such mixed-valence states in parent system, ECMO and TCMO, have already been observed by the detailed XPS study [50,211]. Thus, we can expect the same for the ETCMO too and hence perfect ordering can't be controlled. We have refined the XRD patterns of ECMO and ETCMO using Rietveld method with the cation-disordered orthorhombic phase (*Pnma*). The insets of Fig. 4.1 are showing the structures of ECMO and ETCMO, extracted by importing crystallographic information file (CIF) to VESTA software. The refinement confirms the existence of single-phase for both samples without any impurity peak. The structural information for the ECMO and ETCMO is described in Table 4.1, while the space group for the parent system TCMO is also the same as has been reported by S L Wang et al [213]. The unit cell volume of ECMO, ETCMO and TCMO is 224.9, 222.9 and 221.2 $Å^3$ respectively. Thus, the cell volume was reduced with increasing Tb concentration.

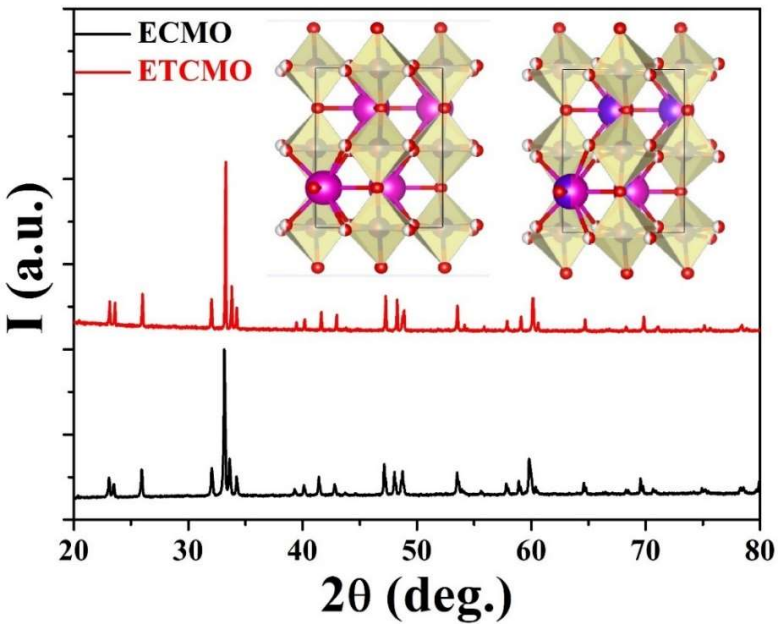

Figure 4.1: *The XRD patterns of ECMO and ETCMO taken at room temperature with insets showing the structures of ECMO (left) and ETCMO (right).*

***Table 4.1**: Structural parameters and crystallographic sites of ECMO and ETCMO estimated from powder XRD patterns at room temperature; Space group: Pnma (62)*

Parameters	ECMO	ETCMO
a	5.5782(10) Å	5.5805(3) Å
b	7.5695(12) Å	7.5373(3) Å
c	5.3260(10) Å	5.2999(3) Å
V	224.8872(32) $Å^3$	222.9239(9) $Å^3$
Eu/Tb site	4c	4c
x	0.0623(2)	0.0652(6)
y	0.25000	0.25000
z	-0.0121(7)	-0.0120(18)
Co/Mn site	4b	4b
x	0.00000	0.00000
y	0.00000	0.00000
z	0.50000	0.50000
O(1) site	4c	4c
x	0.484(2)	0.472(6)
y	0.25000	0.25000
z	0.096(3)	0.109(6)
O(2) site	8d	8d
x	0.267(10)	0.282(15)
y	0.016(7)	0.034(9)
z	0.732(11)	0.729(17)
Chi^2	2.62	2.76
R_{wp}	15.1	34.1
R_{exp}	9.36	20.5
GOF	1.61	1.66

4.3.2 Transport property

The temperature-dependent electrical resistivity (ρ) of ECMO and ETCMO below room temperature is shown in Fig. 4.2(a, b). It has been observed that the resistivity increases with decreasing temperature, showing a semiconductor-like behavior. The variation of the resistivity of both systems, below 200 K can be fitted to the variable range hopping model [19,20,210,226]. This model assumed that at low temperature hopping resistances between neighbors become overweight than those connecting some distant species and only those states participate in conduction whose energies lie in a narrow band especially close to the Fermi level. The equations describing variable range hopping (VRH) is given as,

$$ln\rho = ln\rho_0 + T_0^{1/4}.T^{-1/4} \quad (4.1)$$

Where ρ_0 is a perfector and T_0 is an important parameter for determining the electrical transport properties of the system, known as Mott's characteristics temperature. The parameter, T_0 is related with localization length (1/α) of the wave-function (here α is the inverse of decay length of the localized polaron wavefunction), Boltzmann constant, k_B and the density of localized states, $N(E_F)$ near Fermi level through the relation,

$$T_0 = 24\alpha^3/\pi k_B N(E_F) \quad (4.2)$$

The slope of the fitted line (inset of Fig. 4.2(a, b)) with equation 4.1 was used to determine the numerical values of T_0. The 1/α is approximately equal to the twice of the Co-Mn bond length i.e., the average spacing between adjacent Co or Mn ions [22], which is (3.88 ± 0.12) x10^{-10} m for ECMO and (3.90 ± 0.18) x10^{-10} m for ETCMO. However, in La_2CoMnO_6 (LCMO), Rabindra et. al. assumed the localization length of ~10^{-10} m [226]. Additionally, the polaron

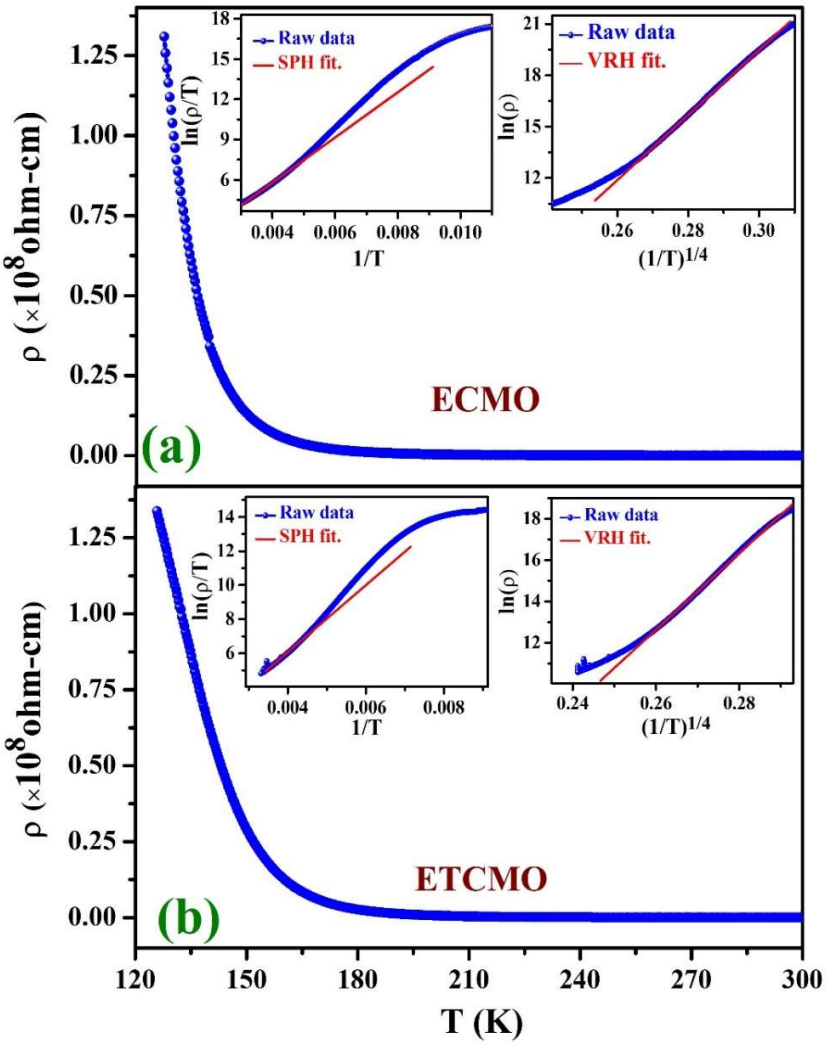

Figure 4.2: *The temperature-dependent resistivity along with insets showing VRH and SPH fitting of (a) ECMO and (b) ETCMO*

Table 4.2: *VRH parameters for ECMO and ETCMO.*

Sample	$T_0^{1/4}$ (K)	$N(E_F)$ ($eV^{-1}m^{-3}$)	W @200 K (eV)	αR
ECMO	164.19	1.90×10^{24}	0.188	76.40
ETCMO	161.71	2.02×10^{24}	0.185	75.24

activation energy (W) at temperature T can be calculated via expression, $W = 0.25\ {k_B T_0}^{0.25} T^{0.75}$, with most probable hopping distance,

$$R = \left[\frac{9}{8\pi\alpha k_B N(E_F)}\right]^{1/4} = \left[\frac{9T_0}{192\alpha^4}\right]^{1/4} \quad (4.3)$$

The value of $N(E_F)$ for both the systems (using equation 4.2) at Fermi level was found to be ~10^{24} $eV^{-1}m^{-3}$, which is of the order of a typical semiconductor oxide. Rabindra et. al. reported the value of $N(E_F)$ in LCMO system of order of ~10^{24} $eV^{-1}m^{-3}$ (i.e., ~10^{18} $eV^{-1}cm^{-3}$) and it is in the range of 10^{23} to 10^{25} $eV^{-1}m^{-3}$ (i.e., 10^{17} to 10^{19} $eV^{-1}cm^{-3}$) for oxide semiconductors [226]. R. Yadav et. al. reported the two values of $N(E_F)$ i.e., 1.695 x 10^{24} $eV^{-1}m^{-3}$ (for the LCMO sintered at 1100° C) and 1.865 x 10^{24} $eV^{-1}m^{-3}$ (for the LCMO sintered at 1200° C) [19]. Thus, the order of $N(E_F)$ of ECMO, ETCMO and LCMO is same. In order to confirm the validity of the VRH model according to Mott, the polaron activation energy W should be greater than thermal energy (k_BT) and most probable hopping distance, R should be such that $\alpha R > 1$ [19]. The computed value of these transport parameters using above equations is summarized in Table 2, implying the validity of Mott's criteria. Thus, similar to other double perovskite systems, like its sister compound LCMO [71], the low-temperature electrical conduction can be explained in ECMO and ETCMO too. At higher temperatures (above 200 K) the resistivity was best fitted by small polaron hopping (SPH), a short-range thermally activated energy process [227,228]. Here resistivity follows the equation $\rho = \rho_0 T exp\,(E_a/k_B T)$, due to increased drift mobility and hopping frequency of the charge. The polaron activation energy (E_a) from SPH fitting was found to be 0.145 ± 0.001 eV and 0.170 ± 0.005 eV for ECMO and ETCMO respectively.

4.3.3 Dielectric property

The thermal variations of real part of dielectric constant (ε′) of ECMO in the range 10-320 K at different frequencies, calculated from the electric capacitance measurement are shown in Fig. 4.3(a). The curves show almost non-dispersive intrinsic polarization nature below 160 K with ε′(T) ~ 90 to 110 symptomatic of that the electric dipole relaxation freeze out and did not follow applied electric signal. Above 160 K, it increases sharply showing usual step like nature. Amusingly, it exhibits mammoth value of low-frequency ε′ (which is ~2500 @5 kHz) at room temperature and decreases at higher frequency owing to dominant probability of intra-well hopping of charge carriers. Besides this, an increase in frequency shifts the step position towards the higher temperature. Such strong frequency dispersion of ε′ near room temperature ascribed to extrinsic polarization probably owing to the Maxwell-Wagner (MW) effect assisted by interfaced depletion layers between sample and contacts or at grain boundaries [229–232]. In a sister compound LCMO, it has been ascribed that the electrically mixed microstructure which is composed of some conducting regions (as a result of ASD) and insulating regions (due to perfect Co/Mn ordering), might be a reason behind the high value of room temperature dielectric constant [233]. The steps, showing a transition from intrinsic to the extrinsic region are associated with a peak in dielectric loss i.e., tanδ curves (Fig 4.3(b)). The measured peak temperature at different frequencies is illustrated in Fig. 4.3(c). The shifting of tanδ-peak towards higher temperature for higher frequency is a sign of thermally activated relaxation phenomenon, which obeys the Arrhenius law, $f = f_0 exp[-E_a/k_B T]$, where $1/f_0 = \tau_0$ is the relaxation time of the dipoles and E_a is the energy required for reorientation of dipolar region known as activation energy. The fitting of equation (6) for ECMO result in activation energy ~ 0.25 ± 0.01 eV with a relaxation time of ~10^{-10} seconds.

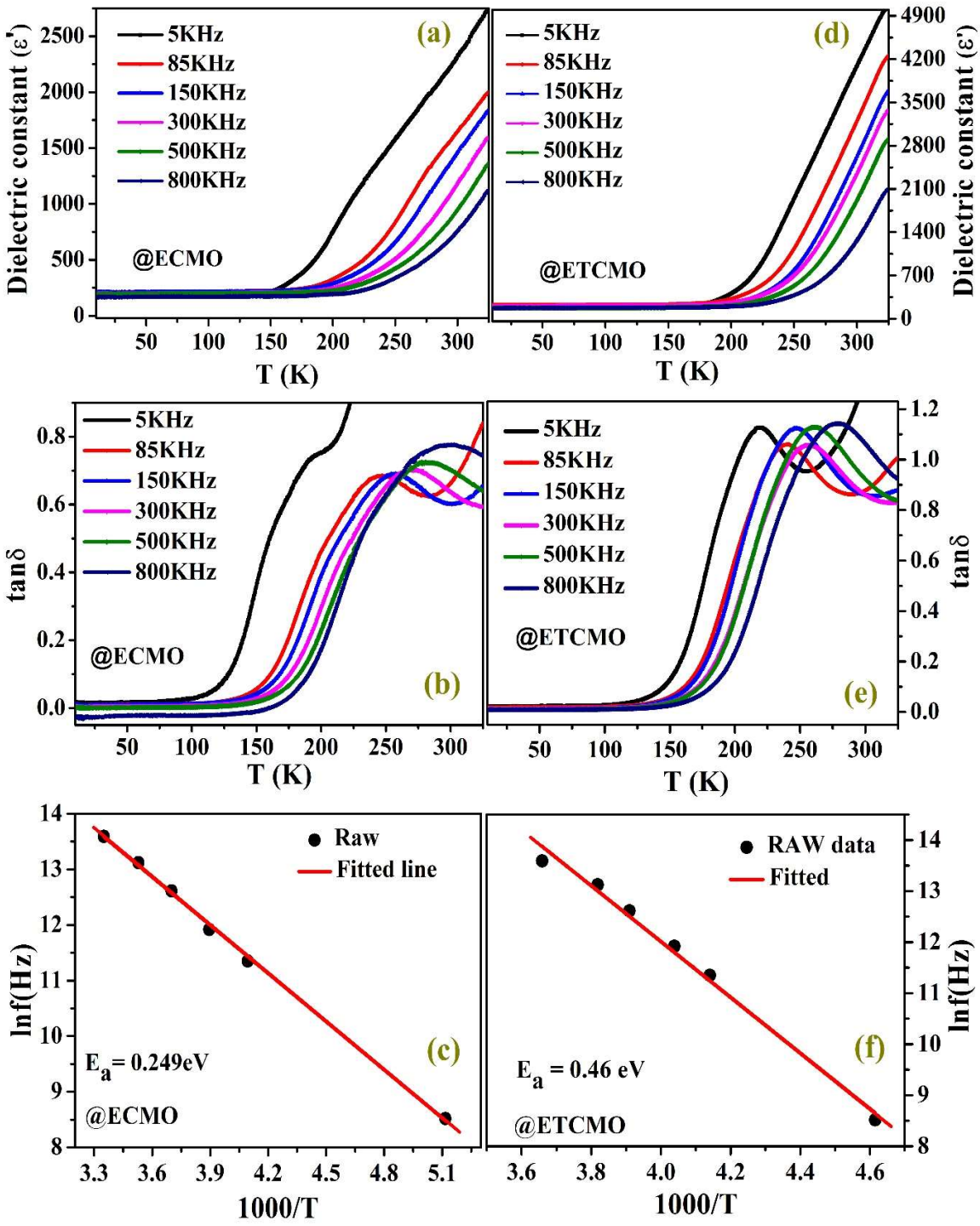

Figure 4.3: *(a, d) The thermal variations of real part of dielectric constant of ECMO and ETCMO & (b, e) the thermal variations of dielectric loss of ECMO and ETCMO at different frequency. (c, f) The relaxation peak temperature at different frequency and Arrhenius law fitting of ECMO and ETCMO.*

Further, Fig. 4.3(d) consists of ε′(T) curves at different frequencies of ETCMO. It can be seen that there is an increased dielectric constant with a colossal value of room temperature ε′ (~4800) at a typical frequency of 5 kHz and enhanced relaxor peak in loss spectrum (Fig. 4.3(e)). These changes are might be due to increased heterogeneity and defects near grain boundary due to Tb substitution. Thus, leads to the increased probability of inter-well hopping which has an effect on the dielectric relaxation mostly at low frequency. However, heterogeneous distribution of the ions may pile-up charge carriers which respond to the external electric field in a different manner giving rise to additional electric polarization [234]. The shifting of loss peak for both the samples suggests that along with the MW relaxation it might be possible that there exist a weak ferroelectric relaxor state which is responsible for the large ε′. But it is not sufficient information to reveal the exact physics behind the dielectric relaxation in these materials and needs further study. Additionally, the step shifts to high temperature at a given frequency for ETCMO similar to the earlier reported Tb doped LCMO system [212]. This is consistent with increase in resistivity of the ETCMO. These characteristic gives an idea to readers about producing controlled dielectric systems via different size atomic doping on A-site. For the ETCMO, the estimated value of the activation energy (E_a) was found to be around 0.46 ± 0.02 eV and that of relaxation time (τ_0) of the order 10^{-14} second using Arrhenius fitting (Fig 4.3(f)). The smaller value of τ_0 implies existence of a faster polarization process in ETCMO.

4.3.4 Magnetic property

Fig. 4.4 contains the temperature dependence of zero-field cooled (ZFC) and field cooled (FC) magnetization (M) of ETCMO, at an applied field of 100 Oe for the range 5-300

K. The data were collected while warming. The magnetization of ECMO has been examined thoroughly in our earlier report [211]. The magnetization increases slowly with decreasing temperature down to 113 K for ETCMO similar to ECMO [211] and TCMO [212–214,235] and it

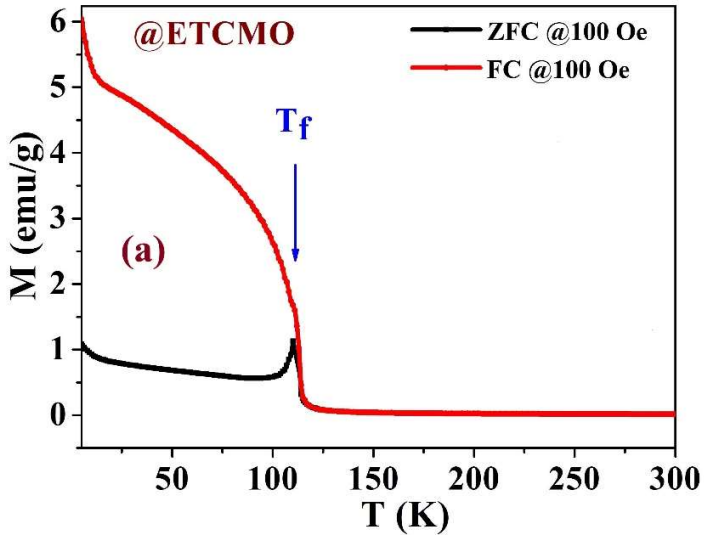

Figure 4.4: *The temperature dependence of ZFC/FC magnetization of ETCMO at 100 Oe applied field.*

increases sharply on further cooling in a ferromagnetic manner. Thus, spontaneous magnetization commences to build up at T_C = 113 K (which is a temperature where dM/dT has a maximum) while for ECMO T_C is around 125 K [211] and for TCMO it is around 98 K [50]. The decrease in T_C with Tb replacement on Eu-site is not surprising as it could be due to a decrease in <Mn-O-Co> bond angle because of the smaller size of Tb^{3+} ion [212]. Just below the transition temperature ZFC curve shows a maximum around the temperature ~111 K for ETCMO), which is a signature of the cobaltites and lightly doped manganites due to strong magnetic anisotropy [77]. The FC curve behaves differently for ECMO, ETCMO and TCMO due to difference in magnetic anisotropies of Eu^{3+} and Tb^{3+}. Below T_C, FC magnetization of

ETCMO increases continuously, tending towards saturation down to 12 K, followed by a large ZFC/FC bifurcation. However, below 12 K again M changes its slope with a sudden increase which keeps up a correspondence to the evolution of short-range magnetic ordering in the Tb sub-lattice [236]. From Fig. 4.5(c), it can be seen that the bifurcation between ZFC/FC and transition temperature (T_C) also increases at higher fields. The temperature where bifurcation in ZFC/FC start is called spin freezing temperature (T_f), suggesting the possibility of a glass transition [83]. Furthermore, the T_f moves towards lower temperature (Fig. 4.5c) at higher applied fields, which is also a signature of glassy dynamics [172–174]. These disguising properties together indicates presence of competing ferro-magnetic (FM) state attributed to Co^{2+}-O^{2-}-Mn^{4+} exchange interactions and anti-ferromagnetic (AFM) state owing to Co^{2+}-O^{2-}-Co^{2+} and Mn^{4+}-O^{2-}-Mn^{4+} interactions in ETCMO similar to its parent system [34,211,237].

Fig. 4.5(a, b) shows the variation of inverse DC susceptibility (χ^{-1}) with temperature at 100 Oe of ECMO and ETCMO. The χ^{-1}(T) varies linearly above 200 K, showing a pure paramagnetic (PM) phase which follows Curie-Weiss (CW) law i.e., $\chi = C/(T - T_{CW})$. From the CW fitting, we have estimated an effective PM moment of 12.4μ_B and CW temperature (T_{CW}) about 48 K for ETCMO. The effective PM moment and T_{CW} for ECMO were estimated to be around 7.7μ_B and 98 K for ECMO [211] while it was around 14.9μ_B and 28 K for TCMO [212]. The large difference between T_{CW} and T_C suggests the existence of strong spin frustration. The positive value of T_{CW} signifying that there exists dominating FM interaction. On the other hand, χ^{-1}(T) shows a downturn from the linear behavior below 200 K (T_G). This behavior has been recognized as the formation of small FM clusters in the PM region which is a signature of the Griffiths-like-phase (GP). The existence of GP in ECMO has been reported earlier [122]. In Fig. 4.5(d) χ^{-1}(T) at higher applied fields have been presented. In GP, the

downturn of χ^{-1}(T) should gradually soften as we move towards higher fields due to rising of PM background which covered the FM signal. The spins are ferromagnetically correlated only within those small clusters while the system as a whole has neither long-range ordering in GP nor spontaneous magnetization [103,238–240].

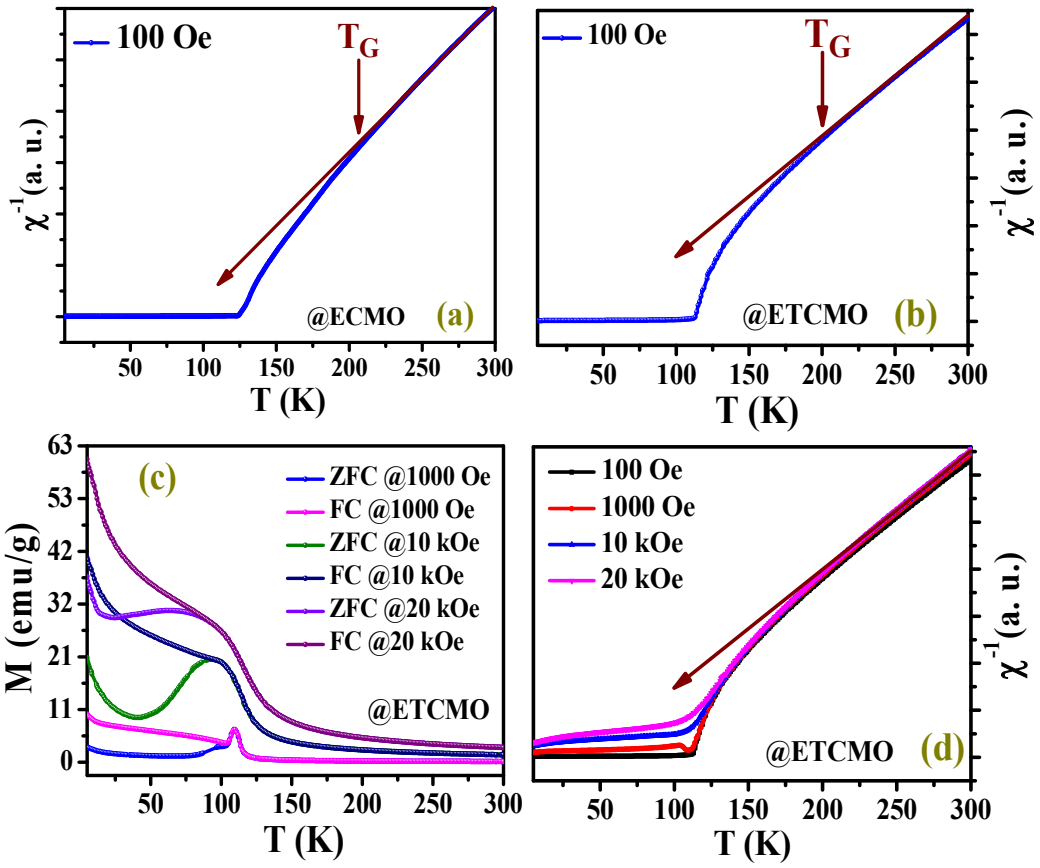

Figure 4.5: *(a, b) The variation of inverse DC susceptibility with temperature at 100 Oe of ECMO and ETCMO. (c, d) The variation of ZFC magnetization and inverse DC susceptibility of ETCMO at higher applied fields.*

Critical behavior studies are a very powerful means for in-depth analyses of nature of magnetic transitions [48, 91]. To examine the critical exponents (δ, γ, β) associated with long-range magnetic transition, we have measured closely spaced isothermal magnetization around

T_C (see Fig. 4.6(a)). In the vicinity of II-order transition, the microscopic nature of magnetization is described by the universal scaling hypothesis where magnetization at T_C (M(H)), M_S (spontaneous magnetization), and χ_0 (initial susceptibility) diverges as [122,240],

$$M_S(0,t) \sim (-t)^{\beta}, t < 0 \quad (4.4)$$

$$\chi_0^{-1}(0,t) \sim (t)^{\gamma}, t > 0 \quad (4.5)$$

$$M(H,0) \sim (H)^{1/\delta}, t = 0 \quad (4.6)$$

Where, $t = (T - T_C)/T_C$ is the reduced temperature and the exponents δ, γ and β are related with each other via the Widom scaling relation, i.e., $\delta = 1 + \gamma/\beta$.

The above-described power-law fitting to M_S and χ_0^{-1} (shown in Fig. 6(c, d)) for ETCMO gives value of β = 0.86 ± 0.02 and γ = 1.35 ± 0.03. Using Widom scaling relation, the value of δ is calculated to be 2.57 ± 0.1. Further, the exponent δ has been estimated using the log-log plot of the M(H) isotherm at T = 112 K (Fig. 4.6(b)) which is nearest to critical isotherm and is found to be 2.45 ± 0.01. Thus, the obtained values of δ using the log-log plot are consistent with Widom scaling relation for ETCMO. The value of δ should be near or greater than 3 (as it is 3.0 for Mean Field Model, 4.8 for 3D Heisenberg Model, 4.82 for 3D Ising Model and 5 for Tri-critical mean-field model) to follow existing conventional scaling theory [122]. The value of δ for ETCMO is small and closest universal scaling hypothesis is the mean-field theory. Much smaller value of δ (around 1.55 ± 0.03) was found in Gd_2CoMnO_6 and it is reported that such a small value of δ is attributed to slow continuous ordering, which is usually for non-Griffiths-like cluster formation [240]. The critical behavior in the ECMO was

systematically investigated by Y. Jia et al [122] and the critical parameters (β, γ and δ) were estimated to be around 0.6065, 0.9237 and 2.52, close to the mean-field theory.

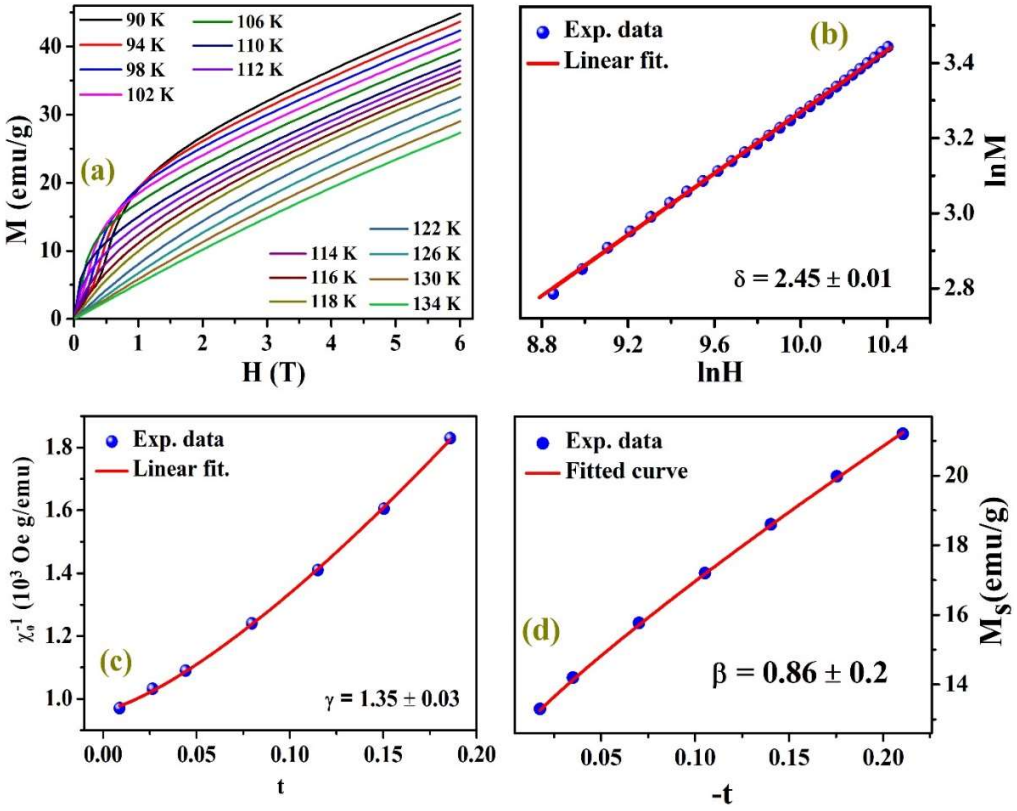

Figure 4.6: *(a) The isothermal magnetization curves around T_C (b) The variation of lnM vs. lnH, (c) The inverse initial susceptibility vs. reduced temperature and (d) The spontaneous magnetization vs. reduced temperature of ETCMO.*

Furthermore, the estimated critical exponents can be visualized through magnetocaloric effect (MCE) analysis. The physical quantity associated with the MCE is the magnetic entropy change ΔS_M, which can be calculated using magnetization measurement under the application of magnetic field at different temperatures as has been described in several reports [210,240]. The calculated values of ΔS_M as a function of temperature in the vicinity of phase transition for different magnetic fields for ETCMO have been presented in Fig. 4.7(a). It can be seen that

$\Delta S_M(T)$ shows a maximum value (ΔS_M^{Max}) around magnetic transition temperature T_C with a maximum value ~2.3 J/kg-K for an applied field of 5 T. The maximum value of ΔS_M^{Max} for ETCMO is of the same order of ECMO (~2.5 J/kg-K for an applied field of 5 T) [210]. J. K. Murthy et al, observe a low-temperature giant magnetocaloric performance in Gd_2NiMnO_6 (ΔS_M^{Max} ~ 35.5 J/kg-K) and Gd_2CoMnO_6 (ΔS_M^{Max} ~ 24 J/kg-K) for the magnetic field of 0–7 T [47]. Many other A_2(Ni, Co)MnO_6 DPs (A = Tb, Gd, Ho, Dy, Pr, Er and Nd) are also have

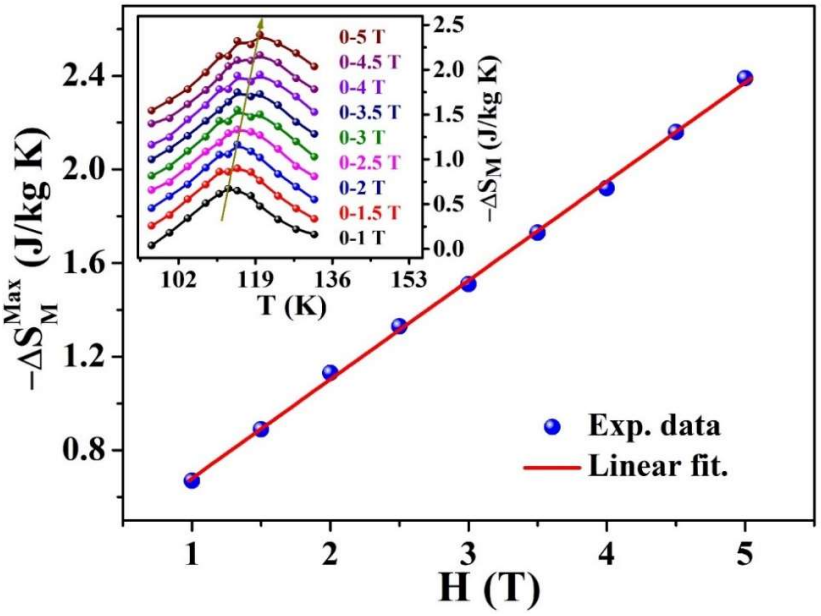

Figure 4.7: *Variation of maximum magnetic entropy change with magnetic fields and inset is showing magnetic entropy changes at different temperature in different magnetic field.*

been reported with a large MCE at low temperature [8,203,241,242]. The ΔS_M^{Max} varies with magnetic field (H) as a power law given by [243],

$$\Delta S_M^{Max} \approx H^n \tag{4.7}$$

Where the exponent n and critical exponents β & γ are related with each other according to the Arrott-Noakes relation as [240],

$$n = 1 + [\beta - 1]/[\beta + \gamma] \quad (4.8)$$

To find out the value of "n" for ETCMO, we have plotted the variation of ΔS_M^{Max} with H, as has been shown in Fig. 4.7(b). It has been observed that the ΔS_M^{Max} varies almost linearly with the magnetic field, thus n is nearly equal to 1. Furthermore, using equation (4.8) we found the value of n ~ 0.94, suggesting a good agreement of the above-mentioned experimental value, thus the critical exponents are explicit and self-consistent.

The magnetizations vs. field (MH) curves of ETCMO at 5K, 100 K, 150 K and 300 K are shown in Fig. 8. At lower temperature (5 K) this magnetization isotherm shows a clear FM hysteresis loop and does not achieve saturation up to applied field of H = 7 T. The un-saturation of isothermal magnetization again suggests the existence of competing FM and AFM interaction due to disordering in the system which can be explained by Goodenough-Kanamori rules [34,237]. ETCMO shows a very weak signature of single stepped MMT at lower temperature which is marked with arrow in Fig. 4.8. Here observed MMT might be due to anti-alignment of Tb^{3+} spins with Co/Mn sub-lattice which is seen in our M(T) at lower temperature [7]. The magnitude of magnetization of ETCMO is enlarged than the expected value of perfect polarized Co/Mn-sublattice at higher field. Thus Tb-sublattice also contributes in FM ordering, which is proven using neutron diffraction study [212]. However, at 100 K, ETCMO shows weak hysteresis and significance MMT similar to ECMO. Thus, suggesting that Eu^{3+}/Tb^{3+} do not play major role at higher temperatures and leading contributions come from the Co-O-Mn exchange interaction path. The observed MMT might be attributed to spin flopping and martensitic-like transition, which causes a transition from AFM to FM states under influence of an external magnetic field. The isothermal magnetization curves at 150 K and 300 K shows

linear variation with an applied field which certified to PM state. The magnitude of the magnetization at 150 K is larger than that of 300 K due to lesser thermal fluctuations and clustered phases as well.

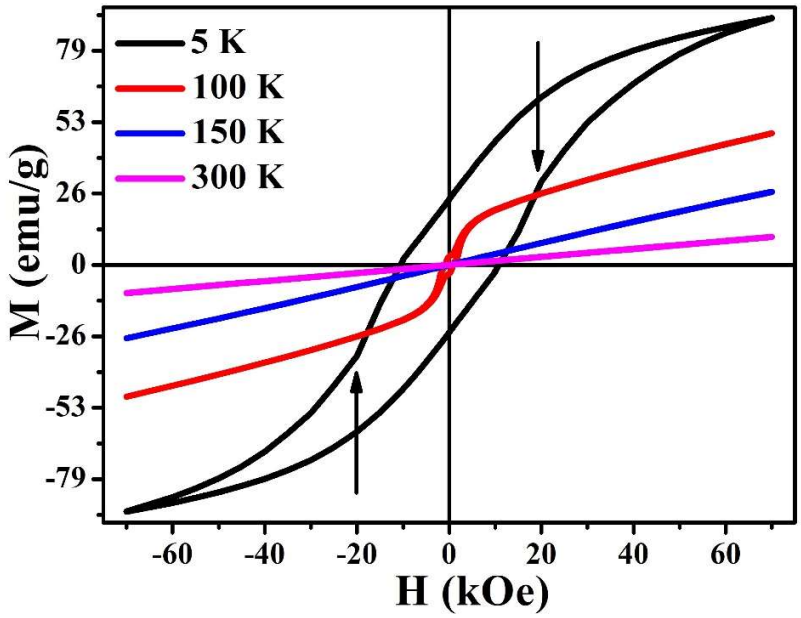

Figure 4.8: *The isothermal M(H) curves of ETCMO at 5K, 100 K, 150 K and 300 K respectively.*

4.4 Conclusion

The detailed analysis of XRD, resistivity, dielectric and magnetic properties of ECMO and ETCMO were studied comparatively. The Rietveld analysis of powder diffraction pattern shows all the peaks of both the samples can be indexed to a single disordered orthorhombic phase with space group *Pnma*. The variations of resistivity were fitted to VRH and SPH models. The estimated VRH parameter satisfies Mott's criterion and confirms the semiconducting nature of both systems. Interestingly, they have a very high ε′ at lower frequency near room temperature and show strong frequency dispersion. On decreasing

temperature, the ε′ decreases sharply to a lower value, which is attributed to extrinsic to intrinsic transition. The loss spectrum exhibits a frequency-dependent peak which is generalized as a thermally activated phenomenon. Moreover, shifting of steps for a given frequency with Tb replacement is motivational for us for technological application. The MT measurement shows that the transition temperature has been decreased with Tb replacement on Eu-site. Moreover, the inverse DC susceptibility of ETCMO and its evolution with applied magnetic field shows a ferromagnetic-clustered phase in PM region. The study of critical exponents shows that critical parameters are close to the parameters which are obtained by the mean-field theory. A large difference between T_C and T_{CW} as well as ZFC/FC bifurcation was observed, which suggests strong spin frustration is present in our system. Low-temperature MH curve of ETCMO exhibits FM nature along with a weak MMT in contrast to our previously reported sharp field-induced MMT in ECMO.